

NEUROPIXEL DATA TO 3D VISUALISATION

4509 Group project - Imperial PixelMinds

**Department of Bioengineering
Imperial College London**

*A Project Report Submitted in
Partial Fulfilment of the*

MEng Biomedical Engineering / Molecular Bioengineering / Bsc Medicine Degree

Supervisor:
Clopath, Claudia

Department of Bioengineering
c.clopath@imperial.ac.uk

April, 2025

NEUROPIXEL DATA TO 3D VISUALISATION

Kangjun Ji, Migliorini Vittorio, Yihan Zhao, Zhuoling Shi, Chang Su, Ming Zhu,
Nancy He

April 14, 2025

Abstract

Most neuroscientists still carry out manual spike sorting and post-hoc histological reconstruction to identify neuron types and anatomical locations. This labor-intensive task often produces a high incidence of artefacts, likely caused by tearing of tissue and debris, which leads to inaccurate reconstruction of the brain's 3D structure. [1]. This project addresses the need for a simplified computational pipeline that classifies neuron types and localises their activity within the mouse brain, using high-density Neuropixel (NP) recordings. Building on the distributed work presented by Steinmetz et al. [2], our streamlined process first identifies neuron function categories, such as vision, action, and choice-selective, through a nested test classification algorithm. Following this, it determines Peak-to-Peak (PTP) spike localisation parameters using gradient descent, allowing for an estimate of spike localisation. By incorporating a three-dimensional mouse brain atlas, we can visualize the anatomical distribution of neuron types and highlight how specific neurons for sensory inputs, decision formation, and motor responses span multiple brain structures, underscoring collaboration between brain areas and intracortical pathways. In initial evaluations with publicly available NP data [2], our pipeline replicated anatomical locations of spike data, originally discerned by the authors via post-hoc histological reconstruction. Our pipeline offers a streamlined approach for rapid data processing, classification, and anatomical display, facilitating broader exploration of neuron population interactions. We predict that our method can enable researchers to perform more efficient large-scale analyses of neural mapping, potentially aiding the discovery of unknown neurological pathways that underlie complex behaviours in health and disease.

1 Introduction

1.1 Neuron Encoding

Understanding how the mammalian brain encodes behaviour, cognition, and sensory processing is dependent on identifying where and how different neuron types fire under specific conditions. Neurons can exhibit distinct functions, such as action-related neurons that respond broadly to motor events, vision-specific neurons stimulated by sensory input, and choice-selective neurons that predict the direction or outcome of a decision [2]. Mapping that diversity onto the corresponding brain circuits remains a distinct challenge in neuroscience [3], particularly given

that these coding patterns are often spread through multiple brain regions rather than localising to small, isolated structures [2].

1.2 Neuropixel Probes

NP probes, advanced high-density recording devices built on CMOS technology, provide an abundance of neural data including both spike voltages and detailed x and z coordinates that map neural activity location along the probe's shank [4]. This rich dataset allows for the capture of complex spatiotemporal patterns in neuronal firing [4]. However, the built-in two-dimensional nature of data complicates efforts to accurately translate spike events into three-dimensional (x , y , z) space

[4], a critical step when attempting to display neural activity onto a 3D model of the brain. This complexity requires innovative computational approaches, to handle partial 2D data (x, z), and precise calibration to ensure that the spatial mapping of neuronal spikes is both accurate and dependable for advanced neuroscientific studies. Furthermore, the intrinsic structure and data of NPs introduces its own complications, probe drift being a key, NP-related, obstacle where small mechanical movements or tissue deviations can cause neurons to shift relative to the probe, degrading spike sorting quality over time [5]. Additionally, the physical insertion of the probe can create slight alignment changes or tissue compression, further complicating the process of assigning neuron clusters to specific anatomical coordinates [5]. Modern spike-sorting algorithms, for example, Kilosort, are able to compensate for this drift by modelling the probe's changing position, via a mathematical model, tracking how waveforms at each electrode change over time [6] but the process can still be rather time consuming.

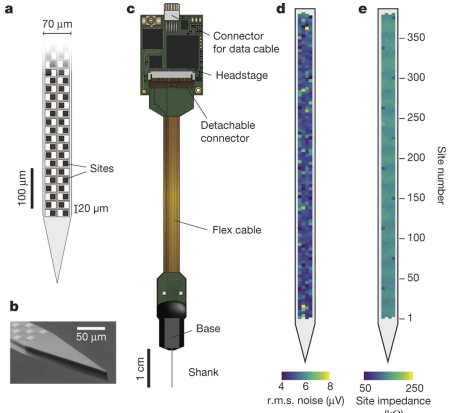


Figure 1: NP probes with their precise design and properties. (a) Layout of electrode structure and electrode sizes. (b) Electron micrograph of probe tip. (c) Entire probe assembly with headstage, connector, flex cable, base, and shank. (d) Illustration of electrode site distribution of root mean square (r.m.s.) noise. (e) Illustration of electrode impedance distribution. [7].

1.3 Current State of Brain Mapping

Most recently, researchers have relied on methods such as post-hoc histology and manual spike classification to pinpoint neuron locations and determine their firing properties [2]. These approaches, although producing important findings, require considerable time and resources due to the need for animal sacrifice, manual reconstruction of brain slices, and painstakingly matching electrode tracks to anatomical reference atlases (physical tracks created from probe insertion/removal)[2]. Furthermore, real-time feedback on experimental design is difficult to obtain due to delays required for histological processing, limiting

researchers' adaptability in experiments[8]. Modern computational methods, such as those introduced by Boussard et al., have been introduced as an alternative to these limitations. Instead of relying on manual histological reconstruction, these approaches use computational tools to localise spikes more efficiently and accurately.

1.4 Main Objective

As discussed, NP data analysis frequently involves a number of disconnected, highly specialised steps, ranging from raw signal preprocessing to neural spike localisation, neuron classification, and final visualisation – each of which can be quite time-consuming and with limited adaptability. Our project addresses these issues by proposing a streamlined coding pipeline that;

- (i) Identifies neuron types based on a kernel function, employing a nested test to categorise cells into action-, vision-, or choice-related subtypes.
- (ii) Localises firing clusters in three dimensions using gradient descent-optimised parameters.
- (iii) Displays the results on an interactive 3D mouse brain model.

Our overall goal is to demonstrate both the feasibility and use of a generalisable code-pipeline that bridges modern NP electrophysiology with its anatomical context via visual inspection.

2 Background

2.1 Framework for Brain-Wide Functional Neuron Labeling

Steinmetz utilised high-density NPs probes to record from hundreds and thousands of neurons across 42 brain regions in behaving mice, verifying that sensory perception, motor planning, and decision-making are supported by distributed neural activity across the entire brain [2]. Their behavioural task allowed spike trains to be temporally segmented into stimulus-driven, pre-movement, and post-movement phases, facilitating fine-grained functional analysis. During the experiment, mice performed a two-alternative and Go-NoGo task that required them to report the location of a visual stimulus by turning a steering wheel, or not moving when no stimulus was presented (Figure 2).

Importantly, it also allowed the dissociation of neural correlates of sensory processing, motor initiation, and action selection. Using spike sorting (Kilosort) and anatomical localisation via histological reconstruction, the authors recorded over 29,000 neurons, with more

than 22,000 neurons mapped to specific brain regions. Steinmetz et al. applied these neurons into three major types: vision-related, choice-selective, and action-related respectively. Each neuron's spike train was convolved with temporal kernels corresponding to distinct behavioural epochs, and neurons were labelled by different functions based on the significance of their firing patterns in comparison to shuffled controls.

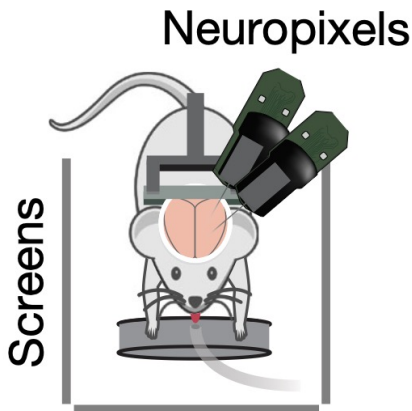


Figure 2: Schematic illustration of a mouse undergoing a typical NP recording setup, showing dual NP probes inserted into the brain to record neuronal activity. The mouse is positioned facing screens used for visual stimulus presentation, as described by Steinmetz et al. (2019).[2].

2.2 Computational Limitations in Spike Localising

Based on the experimental framework established by Steinmetz [2], Neuron spike localisation was primarily achieved across post hoc histological reconstruction. Typically, NP probes provided spike recordings with voltage recordings and associated spatial coordinates (x, z) along the probe shank, and identified in histological brain sections by using fluorescently labelled prob tracks and Allen Mouse Brain Atlas [9]. While precise, this method has inherent limitations: it requires animal sacrifice, complex tissue processing, and error-prone manual alignment due to tissue distortion. Probe drift during extended recordings further compromises anatomical accuracy. In order to overcome these limitations, recent computational methodologies have been developed, which enable to estimation of three-dimensional neuron spike localisation directly from electrophysiological data. Specifically, the computational method called PTP amplitudes of spike waveforms was developed. As showed in the equation (4), there are three axis to regulate coordinations. The PTP method optimizes spike localisation in three-dimensional space (x, y, z), which increases lateral (Y-axis) information making the positioning of neurons in three-dimensional space more accurate and complete

[4]. This is shown in Equation (4).

3 Methods

In this section, we describe the procedures, methods, and analytical techniques applied for the data analysis, such as spike filtering, kernel regression techniques, and spike visualisation (Figure 3). The dataset that we have used for this project is openly available from Steinmetz et al [2].

3.1 Filtering

3.1.1 Individual Spike Filtering

The filtering process used in this project involved a series of steps to refine and prepare the raw NP spike data for analysis. First, spike events were selected based on their timing—specifically, when they occurred during each trial. After that, each spike was matched to a cluster ID, making it possible to identify which neuron it came from. In order to best replicate the results of Steinmetz et al., to confirm our filtering accuracy, we focused exclusively on neurons identified within the "SUB" anatomical location. These neurons underwent additional quality filtering to retain only spikes from neuronal clusters rated as "good." This quality filtering was based on a rating system where cluster reliability was classified as either a 1, 2 or 3 with only values of 2 and 3 being "good". Thus, minimising artifacts and noise contamination.

Furthermore, individual neuron selection was based on a series of statistical tests comparing neuron firing rates during distinct event-related windows (such as, stimulus presentation and onset of wheel movement) against baseline firing. Wilcoxon signed-rank tests and rank-sum tests were used to identify neurons showing statistically significant changes in activity ($p < 0.05$). This step helped ensure that only neurons with a clear response to the stimuli were advanced further in the analysis pipeline.

The trial data were further organised into their corresponding hemispheres relative to stimulus presentation, with contralateral being defined as trials where the visual stimulus was presented on the opposite side of the recorded hemisphere, and ipsilateral defined as trials with stimulus presented on same side of the hemisphere being recorded. Additionally, analyses only included trials where the subject made correct responses (wheel movement in the same direction as side of stimulus). This step was carried out in order to ensure data consistency and minimising variability to best compare our results with steinmetz et al.

3.1.2 Visualising Neuronal Firing

Following neuron selection, spikes were aligned in time to specific experimental events, in this case, onset of visual stimuli ($t=0$). Spike counts were then calculated within defined time windows of -0.2s to 0.4s from visual stimuli presentation. To reduce the influence of noise and trial-to-trial variability, we applied a causal half-Gaussian filter with a standard deviation of 0.020 seconds.

For specifically visualisation purposes, Peri-Stimulus Time Histograms (PSTHs) underwent an additional smoothing step, where a second causal half-Gaussian filter with a standard deviation of 0.030 seconds was applied. However, this second smoothing was purely for enhancing visual inspection of PSTHs and was not used in the following analytical steps.

Thereafter, normalisation of firing rates was achieved by subtracting baseline firing activity, measured in the pre-stimulus period (-0.2s – 0.0s), from firing rates at every time point (0.0s – 0.4s).

$$\text{Normalized PSTH}(t) = \frac{\text{PSTH}(t) - \text{Baseline mean}}{\text{Baseline mean} + 0.5} \quad (1)$$

3.2 Neuron Selectivity

3.2.1 Toeplitz Matrix Structure

We constructed predictor matrices to capture how neuron activity corresponds temporally with specific events (visual stimuli, wheel movements, and choices) using a Toeplitz matrix approach [10]:

- **Visual Predictors:** We constructed individual binary matrices for each of six various visual contrast conditions (High, Medium, Low, for Ipsilateral and Contralateral). Each matrix spanned a time window from -0.05 seconds to 0.4 seconds around onset of the visual stimulus. Each point in these matrices specifies whether or not the stimulus was present at that particular lag from the present moment. An entry of "1" indicates that the stimulus was present exactly at that lag, and an entry of "0" means that no stimulus was present (Appendix: Figure 12).
- **Action Predictors:** Similar binary matrices were constructed for motor events (when the mouse initiates a wheel turn). These matrices covered a window from -0.25 seconds to 0.025 seconds relative to the beginning of movement, describing precisely when motor events occurred in relation to neuron activity.
- **Choice Predictors:** We also constructed choice predictors, in a similar fashion to the action predictors, however, these matrices included additional

weighting based on the mouse's choice of direction (left or right). The weighting allows the regression model to capture any differences in neuron response specifically related to the direction chosen by the mouse.

3.2.2 Kernel Regression Model

To measure how much each predictor affected neuron firing, we used an ElasticNet regression model [11] [12]. This method combines two types of regularisation techniques:

- L1 : This allows the model to minimise the impact of less important predictors by reducing their influence to zero, thereby simplifying the model.
- L2: This helps keep the model stable by "spreading" predictor importance evenly, which is useful when certain predictors are highly correlated, hence, reducing the influence of multicollinearity.

Before fitting the model, we combined all predictor matrices (visual, action, and choice) in a side-by-side, horizontal fashion, creating one large predictor matrix containing approximately 650 predictors.

We used 5-fold cross-validation to select the best hyperparameters (regularisation strength α and the mixing parameter ρ), which controls the balance between L1 and L2 penalties).

Cross-validation was done by splitting the dataset into five equal parts. The model was trained on four parts for every round, using the fifth part for testing. This was repeated five times so that each part was a test component just once. This makes sure that our selected model hyperparameters not only perform well on our training data but also adapt well to future data.

With optimal hyperparameters being selected, we applied a final ElasticNet regression model (Equation 2) to our entire dataset. This permitted us to estimate regression coefficients (kernels). Each neuron was assigned its own set of kernels, clearly showing how strongly its firing rate was influenced by different event types: Vision, action, choice.

$$\frac{1}{2n} \|y - X\beta\|_2^2 + \alpha\rho \sum_{j=1}^p |\beta_j| + \frac{\alpha(1-\rho)}{2} \sum_{j=1}^p \beta_j^2 \quad (2)$$

An explanation of all variables is provided in Table 2 located in appendix.

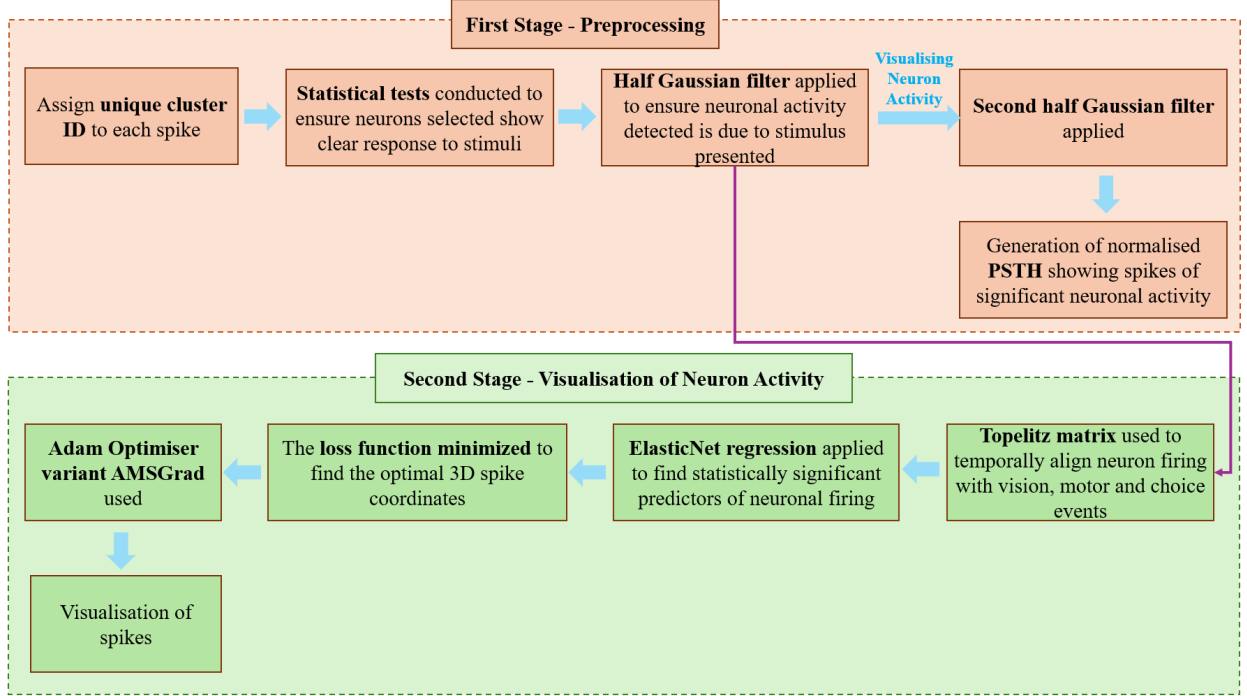


Figure 3: Overall process of the neuronal activity visualisation pipeline, structured in two principal stages. Preprocessing involves filtering based on spikes by their quality, performing statistical tests to identify responsive neurons, and employing Gaussian smoothness filters, initially for analysis and secondarily for exclusively visualisation purposes (Peri-Stimulus Time Histograms, PSTHs). The second stage (Visualisation of Neuron Activity) involved temporally aligning firing of neurons with task-related events by utilising Toeplitz matrices, determining statistically significant predictors with ElasticNet regression, and finally employing an AMSGrad version of an Adam optimiser to optimise loss function for precise 3D spike localisation and visualisation.

3.2.3 Neuron Classification

To determine if a neuron was selectively responsive to a specific event type, we applied a nested permutation test, which involved the following steps;

- Fit the full model: We first fit a model including all predictors to the neuron firing rate data.
- Remove specific predictors and refit: Next, we systematically removed one predictor set (such as, all action-related predictors) and refit the model. If the accuracy of the model significantly decreased (measured as a drop in cross-validated variance), this suggested that the removed predictors were important for explaining neuronal firing.

To carefully test for statistical significance, we used a permutation test. In this process, we randomly shuffled the predictor columns across trials 100 times.

We considered a neuron to be selective if two conditions were met:

- Removing the predictor set led to at least a 2% point drop in variance explained.

- That drop was statistically significant, with a p-value below 0.05.

This approach helped ensure that we only identified neurons that showed true selectivity to visual stimuli, motor actions, or choices.

3.3 Visualisation of the Spikes

3.3.1 Peak-To-Peak Amplitude Calculation

The crucial aspect of spike localisation is determining the PTP amplitude of the action potential for the individual neuron on the particular channel. The maximum and minimum values of the cluster waveforms are demonstrated. The `np.load` is employed to retrieve the template waveforms, along with their corresponding channel index information, from the relevant `.npy` data files. Every cluster is identified by an unique index and contains the waveforms recorded by several channels. By modifying this unique index in the script, the waveforms for different clusters can be accessed. `np.max` and `np.min` are utilised to obtain the peak and trough values of the cluster waveforms, where the PTP amplitude is computed through the equation(3);

$$\text{PTP} = \text{Peak value} - \text{Trough value} \quad (3)$$

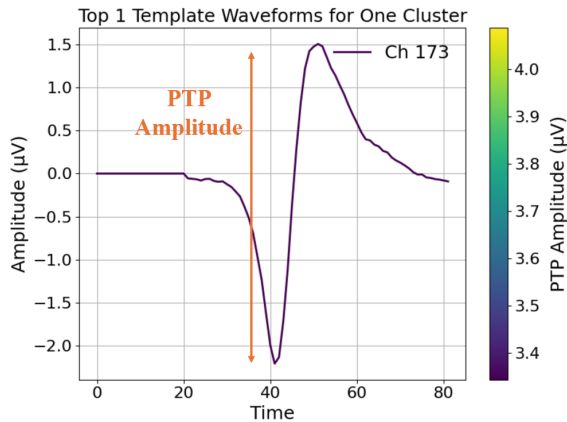


Figure 4: Example waveform showing the measurement of the (PTP) amplitude of a single-cluster neuronal spike recorded on one channel (Channel 173). The colour scale indicates the magnitude of the PTP amplitude in microvolts (μV).

3.3.2 Organization of the Dataset

The Python script is written to compute PTP amplitude for each channel in each cluster at each provided data folder. However, the sequence of channels in the data folder is ordered in arbitrary sequence. Therefore, the other Python script is utilised to order the channel index in increasing order. The expected output of the organization procedure is to order channel index in increasing numerical order, where the corresponding x_c , y_c , and PTP of the channels are also matched with the channel index (Figure 5).

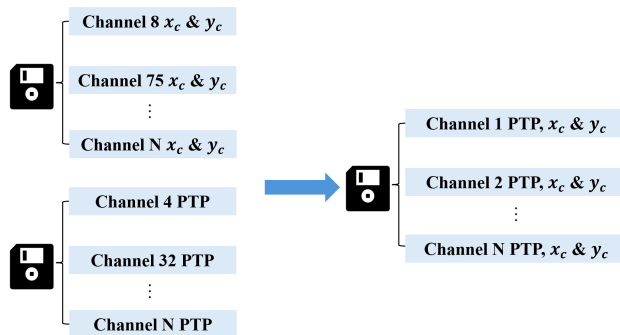


Figure 5: Overview of the data organising process, where channel index data with their respective spatial coordinates (x_c , y_c), along with their corresponding PTP amplitude values, are merged and rearranged into a single dataset with numerical ordering.

The local coordinates of the channels with respect to the NP probes are also provided in the dataset in the form of x_c and y_c , where x_c denotes as the x-coordinate of the channel in a 2D Cartesian coordinate system, and y_c denotes as the y-coordinate of the channel in a 2D Cartesian coordinate system. By combining these data, the pre-filtering procedure is completed, where

the information about channel index, channel PTP amplitude, and channel x_c and y_c coordinates are saved properly for training in the next stage.

3.3.3 Initial Spike localisation Formula

The inspiration of the spike localisation comes from method introduced by [4], which is computed as equation (4), where \mathcal{L} is the total loss for the spike localisation formula, c denotes for the channel index, ptp_c is the PTP amplitude of the spike, and x_c and y_c are provided Cartesian coordinates in the dataset, which denotes for the local coordinates of the spikes relative to the NP probes. By applying the technique of linear gradient descent, the global coordinate of the spikes in the Cartesian coordinates can be visualised in the form of x , y , and z .

$$\mathcal{L} = \sum_{c \in \mathcal{C}} \left(\text{ptp}_c - \frac{\alpha}{\sqrt{(x - x_c)^2 + (y - y_c)^2 + z^2}} \right)^2 \quad (4)$$

$$x \leftarrow x - \eta \frac{\partial \mathcal{L}}{\partial x} \quad (5)$$

$$y \leftarrow y - \eta \frac{\partial \mathcal{L}}{\partial y} \quad (6)$$

$$z \leftarrow z - \eta \frac{\partial \mathcal{L}}{\partial z} \quad (7)$$

$$\alpha \leftarrow \alpha - \eta \frac{\partial \mathcal{L}}{\partial \alpha} \quad (8)$$

Equations (5)–(8) reflect the updating processes of the global Cartesian coordinates x , y , z , and α , where \mathcal{L} is the total loss, η is the learning rate. The optimal global Cartesian coordinates in the form of x , y , and z can be obtained by finding the particular value of x , y , and z and α to make the total loss \mathcal{L} close to 0.

Equation (4) brings significantly essential initial ideas to the spikes visualisation; however, the limitation of equation (4) should not be neglected, which is discussed in detailed in the following section.

3.3.4 Optimisers

After the purely linear gradient method applied to the equation (4), the effectiveness of convergence is unsatisfactory due to the limitation of the purely linear gradient descent on a small-scaled dataset. Therefore, the strategy of utilising the optimisers for improving the convergence effectiveness and performance of the linear gradient descent is implemented.

The Adam optimiser, which is also called the adaptive moment estimation, is an algorithm that can be used to optimise the learning rate in the training of neural network or minimising differentiable functions [13]. It combines the benefits of two conventional methods, including momentum method and RMSProp method, and it simultaneously maintains the moving average of

the gradient (first moment) and the squared gradients (second moment) during the training of the network. The momentum component of the Adam optimiser accelerates the effectiveness of convergence and smooths the updates for each trained parameter, the RMSprop component of the Adam optimiser adapts the learning rate for each trained parameter individually. Equation (9) describes the update process of the Adam optimiser, where θ_t represents the new parameters (x , y , z , and α), θ_{t-1} denotes for the previous parameters, η is the learning rate, \hat{m}_t and \hat{v}_t are the bias-corrected estimates, and ϵ denotes for the small constant that prevents dividing by zero.

$$\theta_t = \theta_{t-1} - \eta \cdot \frac{\hat{m}_t}{\sqrt{\hat{v}_t} + \epsilon} \quad (9)$$

$$\hat{m}_t = \frac{m_t}{1 - \beta_1^t} \quad (10)$$

$$\hat{v}_t = \frac{v_t}{1 - \beta_2^t} \quad (11)$$

Equations (10)–(11) define the relationship for the bias-corrected first moment and second moment estimate, where m_t is the moving average of the first moment, v_t is the moving average of the second moment, and β_1^t and β_2^t are the decay rate for the momentum and RMSprop. However, the Adam optimiser is not the optimal option in this project due to the natural limitation on the learning rate stability and Weak performance for the non-convex problems.

Therefore, the variant version of the Adam optimiser, AMSGrad optimiser, is introduced to improve the convergence stability of effectiveness, solving potential problems caused by non-convex [14]. Equation (12) demonstrates the update process for the AMSGrad optimiser, where θ_t represents the new parameters (x , y , z , and α), θ_{t-1} denotes for the previous parameters, η is the learning rate, m_t is the moving average of the first moment, \hat{v}_t is the bias-corrected estimate for second moment, and ϵ denotes for the small constant that prevents dividing by zero.

$$\theta_t = \theta_{t-1} - \eta \cdot \frac{m_t}{\sqrt{\hat{v}_t} + \epsilon} \quad (12)$$

$$g_t = \nabla_{\theta} \mathcal{L} \quad (13)$$

$$m_t = \beta_1 m_{t-1} + (1 - \beta_1) g_t \quad (14)$$

$$v_t = \beta_2 v_{t-1} + (1 - \beta_2) g_t^2 \quad (15)$$

$$\hat{v}_t = \max(\hat{v}_{t-1}, v_t) \quad (16)$$

Equations (13)–(16) describe the key components of equation (12), where the gradient of the AMSGrad optimiser is computed as shown in equation (13) ($\nabla_{\theta} \mathcal{L}$ denotes the gradient of the total loss \mathcal{L} with respect to the model parameters). The biased first and second moment estimates are computed in equations (14)–(15), and equation (16) maintains the maximum value of \hat{v}_t among all \hat{v}_t values.

3.3.5 Euler-based Spike localisation

During the process of training, the convergence performance of the initially proposed localisation method, denoted as equation (4), converge inefficiently. It reflects that the linear gradient descent method is not optimal approach for this dataset, and the reasons why modified spike localisation method, which bases on the Euler distance, is more suitable for this dataset is discussed in detailed in the discussion section.

Equation (17) computes the improved version of the spike localisation method based on the modification on the Euler model [15] [16], where the Euler distance, z_c denotes for the $\sqrt{(x - x_c)^2 + (y - y_c)^2}$, and the power of 2.5 attenuates the linearity of the linear gradient descent, significantly improving the performance of convergence during the training process. The AMSGrad optimiser is equipped with equation (17) for improving training stability and solving potential problems caused by the non-convex.

$$\mathcal{L} = \left(\sum_{c \in \mathcal{C}} \left(\text{PTP}_c - \frac{\alpha}{\sqrt{(x - x_c)^2 + (y - y_c)^2 + (z - z_c)^2}} \right) \right)^{\frac{5}{2}} \quad (17)$$

3.3.6 Brainrender

In this project, the spikes are visualised through the brainrender, which is an effective tool to visualise spikes in the Allen common coordinate framework (CCF) [17]. Nowadays, fast-evolving AI landscape and LLM-driven platforms are gradually becoming increasingly popular and competitive, which attract people to utilise them for implementing visualisation task rather than traditional software packages, including the Brainrender. However, the packages provided by the Brainrender contains Allen CCF with labelled cortex regions in the mouse brain, which exactly matches with the requirement of this project. Therefore, the Brainrender is applied for visualisation purpose.

4 Results

4.1 Filtering

Our first main step was to make our filtering pipeline robust. The accuracy of the spike filtering dictated the validity of all following analyses, such as detecting selective neuronal responses. To test our approach, we compared our filtered neuronal spike trains with those initially detected by Steinmetz et al.(2019), who originally displayed definitive neuronal selectivity with regards to certain trial events, such as movement.

Our filtering pipeline correctly selected neurons that showed task-related activity changes, in close agreement with Steinmetz et al.(2019). Similar to their findings, our selected neurons also showed event-aligned

firing rate modulations, validating our filtering procedure. The raster plot generated by our coding pipeline shows neuronal activity aligned specifically to movement events for individual neurons within the SUB brain region. Similar to Steinmetz et al.’s original visualisation, our raster plots clearly differentiate neuronal firing between contralateral and ipsilateral trials. In both the original and our replicated plots, the spike events increase prominently with the wheel movement onset (Figure 7). However, subtle visual differences exist between our raster plots and those presented by Steinmetz et al, mainly as a result of unknown smoothing and binning parameters from the original study. This stage confirms that our preprocessing and filtering methods are robust, accurate, and suitable for more advanced analysis, specifically kernel regression analysis.

4.2 Kernel Regression

Having determined consistent spike filtering, we then applied kernel regression analysis to examine neuronal selectivity, that is to say, whether neurons are triggered by visual, action, or decision based stimuli. This selectivity would suggest specialized neuronal functions vital to understanding complicated behaviors, therefore, this step was key to our analytical process.

Our kernel regression analysis successfully discerned multiple neurons selective for action, vision, and choice. Due to computational limitations, our analysis mainly focused on action-selective neurons, however, a small number of neurons selective for vision and choice were also discerned. Neurons were classified as selective if they showed a significant drop in cross-validated variance explained ($>2\%$ points) with an associated permutation test p-value below 0.05. Action-selective neurons were predominantly localised within regions associated with motor activity, such as the primary motor cortex (MOp) and the secondary somatosensory cortex (SSp), with many achieving cross validated explained variance $>2\%$, matching the established threshold by Steinmetz et al.(Table 1)

Neuron	Variance	Selectivity	Region
1	3.2	Action	MOp
2	2.5	Action	MOp
3	2.7	Action	SSp
4	5.0	Action	MOp

Table 1: Sample of Neurons that displayed Full Cross-Validated Variance & Percentage point drop $>2\%$ and their corresponding Selectivity and Region.

The kernel regression analysis demonstrated strong predictive power in estimating neuron firing rates. This was especially clear when action-related predictors were included in the model. In this particular case (Figure 5), the model demonstrated good alignment with the true recorded firing rates. However, upon re-

moval of action predictors from the full model, a decrease in predictive accuracy was visible, underscoring the significance of the action predictors on the models neuronal firing, thus, indicating that action events were important to modulating the neuron’s firing behaviour.

These observations strongly validated our kernel regression feature of our pipeline, defining neuronal selectivity in accordance with Steinmetz et al.’s observations. Once we had determined neuron selectivity, we next proceeded to visualising these selective neuron spikes within specific brain areas, a key-step to correlating functional neuronal activity with spatial localisation.

4.3 Visualisation of the Spikes

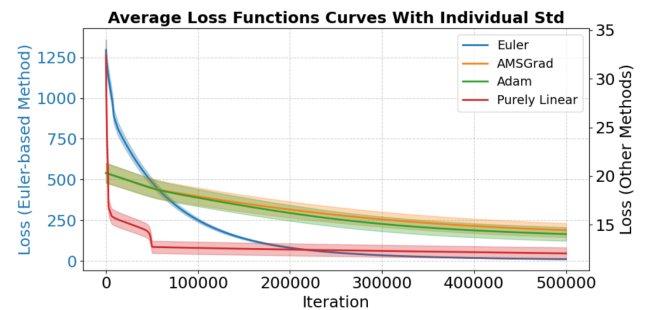


Figure 9: Comparison of average loss function curves over iterations for different optimisation methods (Euler, AMSGrad, Adam, and Purely Linear). Shaded regions represent the standard deviation around each method’s mean loss, indicating variability across individual runs.

Accurate spatial localisation of selective neuronal activity within the brain is essential for understanding brain-wide neuronal interactions. Thus, our final analytical stage involved visualising these selective spikes within a 3D anatomical framework, utilising a Euler-based spike localisation method optimised through gradient descent techniques.

4.3.1 Purely Linear Gradient Descent

It is noticeable that the average total loss starts at roughly 35, and then converges to 10 at 500000 iterations. Although the convergence can be observed, it does not converge effectively for obtaining the optimal spikes coordinate in the global Cartesian coordinate system since the average total loss does not converge to zero. To improve the convergence performance, the Adam optimiser and AMSGrad optimiser are equipped with the linear gradient descent approach.

4.3.2 Linear Gradient Descent with Adam Optimiser

The convergence performance for the linear gradient descent method equipped with the Adam optimiser does not improve significantly, and average total loss converges to approximately 14 at 500000 iterations[13].

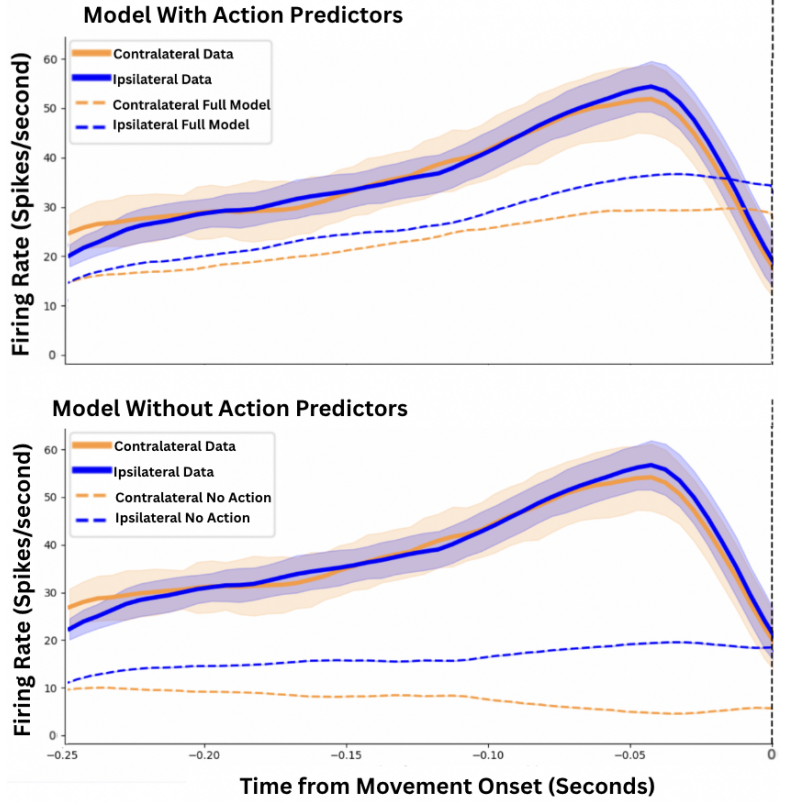


Figure 6: Comparison of Kernel regression model predictions of neuronal firing rates. The top panel displays predicted firing rates (dashed lines) with action predictors included, showing close agreement with recorded firing rates (solid lines) for contralateral and ipsilateral conditions. Predictions from a model with no action predictors in the bottom panel show substantially decreased predictability and display the significant role of action-related events in describing neuronal activity. Shaded areas denote standard error of mean.

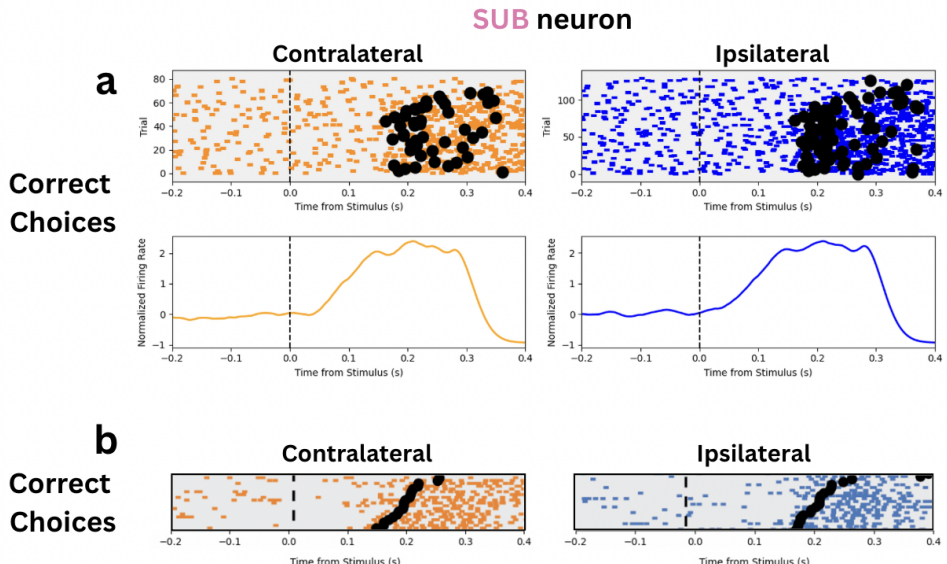
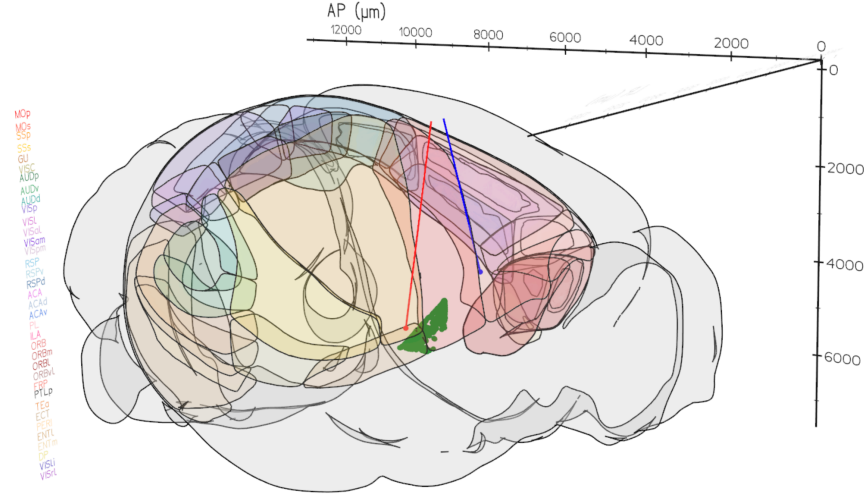


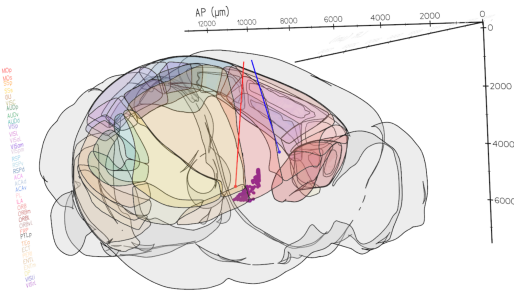
Figure 7: Raster plot and Peri-Stimulus Time Histograms (PSTHs) of neuronal firing activity from one SUB neuron aligned with onset of a visual stimulus (vertical dashed line at 0 s) for correct-choice trials. (a) Raster and PSTH plots from our pipeline, showing neuronal responses for contralateral (left, orange) and ipsilateral (right, blue) conditions. Black circles represent times of wheel movement onset. (b) Equivalent raster plots originally reported by Steinmetz et al. (2019), included for comparison and verification of our findings. Both sets of raster plots demonstrate similar firing increases tightly aligned to movement of mouse during trials.

Visualisation of Spikes in the Mouse Brain



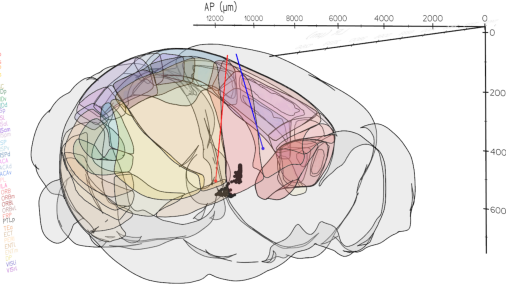
(a) 3D visualisation of regionalised neuronal spikes in the Allen CCF model of the mouse brain. Euler-based localisation of spikes, optimised using AMSGrad, localises recorded spikes accurately in motor-associated areas, specifically the primary motor cortex (MOp) and secondary somatosensory cortex (SSp)

Visualisation of Action Neurons in the Mouse Brain



(b) Visualisation of action-selective neurons within the mouse brain. These neurons, identified through kernel regression analysis, are clearly localised within the motor-related areas, notably the primary motor cortex (MOp) and secondary somatosensory cortex (SSp).

Visualisation of Vision Neurons in the Mouse Brain



(c) Visualisation of vision-selective neurons within the mouse brain. These neurons, although fewer in number, are similarly localised within the motor-related cortical regions (MOp and SSp), which may potentially suggest interaction of these regions during trials.

Figure 8: Neuronal activity visualisations produced by the spike localisation and regression pipeline. Subfigures highlight spike localisation (top), action-selective neurons (bottom-left), and vision-selective neurons (bottom-right).

From the perspective of obtaining the optimal global coordinates for the spikes, the purely linear gradient descent equipped with the Adam optimiser does not fundamentally satisfy the requirement since the average total loss does not converge to zero.

4.3.3 Linear Gradient Descent with AMSGrad optimiser

Although linear gradient descent equipped with the AMSGrad optimiser has better convergence stability than the Adam optimiser, the convergence effectiveness and accuracy is not satisfactory. The dominant reason is concluded that the position of spikes does not distribute linearly. Therefore, a neuron spike localisation method based on Euler model is utilised, and the training overcome is displayed as following.

4.3.4 Euler-based Neuron Spike Localisation

Euler-based neuron spike localisation method equipped with AMSGrad optimiser has noticeable improvement on the convergence effectiveness and accuracy, decaying close to zero with reasonable number of iterations. The average convergence curve has the shape of the exponential decay, which is also expected. Therefore, the Euler-based neuron spike localisation approach with AMSGrad optimiser successfully determine the optimal global coordinates of the spikes in the form of x , y , and z . Although Euler-based neuron spike localisation method equipped with the Adam optimiser also provides similar convergence result, the AMSGrad optimiser is chosen in this project since AMSGrad optimiser ensures the stability convergence at high number of iterations and it can solves the problems caused

by non-convex. Also, it is more suitable for the small dataset that this project uses. Therefore, the Euler-based localisation method with AMSGrad optimiser demonstrates both consistent accuracy and effective minimisation of variability across all methods.

4.3.5 Visualisation of the Spikes in Allen CCF

The optimal coordinates of the spikes in Allen CCF model are visualised in different cortex regions of the brain. The green dots represent the spikes, red and blue straight lines represent the NP probes. The majority of spikes locates at MOp, the primary motor cortex and the SSp, the primary somatosensory cortex. The MOp region is responsible for planning and executing movements [18], which is typically triggered during the behavioural and cognitive neuroscience experiments. Additionally, the SSp region is activated when whiskers and limbs of test subjects move during the experiment (Figure 8a).

The Euler-based neuron spike localisation method accurately localise the spikes in the mouse brain, and the position of spikes in the Allen CCF model statistically accurate describe the data collection process of the experiment, which is discussed in the background.

5 Discussion

5.1 Evaluation of Experimental Design and Alternative Methods

The dataset used in this study comes from Steinmetz et al's work in 2019, using NP probes to extract the neural activities in mice from 29,000 neurons across 42 brain regions. Indeed, mice were chosen due to their genetic similarity to humans, ease for genetic manipulation, and advantages in breeding and cost. Additionally, NP probes capture neuronal activity with millisecond precision and can simultaneously record from several adjacent brain regions. Therefore, the dataset recorded can be used for behavioural studies, including visual, choice, and action neurons. However, such experimental method also has some limitations. Due to its reliance on invasive electrophysiological recording, neuronal localisation can only be determined by histological reconstruction. This necessitates sacrificing the mice while increasing the complexity and labour cost of the operation [19]. Additionally, factors such as probe drift, tissue deformation, and subjective manual spike screening can introduce inconsistencies across experiments. Thus, hindering the accuracy of the results.

5.2 Alternative Approaches

Neuroscience employs a variety of common data acquisition methods rather than a sole reliance on NP probe's electrophysiological recordings. For example,

the patch-clamp method [20] allows more detailed access to subthreshold dynamics, although it is limited to single neurons. Therefore, ideal if the goal is to study a few specific neurons within a larger population. Optical calcium imaging can also simultaneously observe large numbers of neurons and provide anatomical localisation, although the temporal resolution is relatively low and relies on transgenic animals [21]. On the other hand, non-invasive methods such as EEG and fNIRS are suitable for human studies, but lack the spatial resolution at the single-neuron level and NP probes can provide. Indeed, due to the "space vs. time" and "invasiveness vs. scalability" tradeoff [22] [23]. With our aim to study how neurons interact with one other in a behavioural setting, NP probes seem to be the best method. However, sole reliance rather than a combination with several alternate methods is a limitation in this study.

5.3 Filtering Results

The filtering method effectively identified and visualised neurons that responded to task-specific events using Neuropixels data. However, challenges arose when attempting to replicate the original pipeline by Steinmetz et al. (2019), primarily due to the lack of transparency in key methodological parameters such as smoothing kernels and histogram bin sizes [24] [25]. These missing details likely contributed to subtle differences in the selection and classification of neurons. Additionally, differences in programming environments may have affected the outcomes, as their analysis was conducted in MATLAB whereas ours was implemented entirely in Python. Variations in default functions, numerical libraries, and smoothing implementations between platforms could have influenced the results. Nevertheless, Python offered considerable advantages in terms of adaptability and reproducibility. Its widespread use in neuroscience, along with its open-source tools, enabled the development of a flexible and accessible pipeline for future research [26] [27] [28]. However, a limitation of our current approach is that it was applied to a partially pre-processed public dataset rather than raw Neuropixels recordings, which restricts the assessment of its robustness under real-world conditions. A valuable future direction would therefore be to apply the filtering pipeline to completely raw datasets [29] [30], enabling a more comprehensive evaluation of its reliability and generalisability.

5.4 Kernel Results

The recognition of action-selective neurons in the main motor brain regions aligns with the findings by Steinmetz et al. (2019), providing both strong anatomical and methodological validity to our kernel regression procedure. The robust detection of action-selective neurons demonstrates the suitability of our method-

ology. Furthermore, the decision to proceed with ElasticNet regression rather than the reduced-rank regression approach [31] used by Steinmetz et al. (2019) was propelled by ElasticNet’s ability to balance L1 (Lasso) and L2 (Ridge) regularisation. This balance effectively overcomes multicollinearity—common in neuronal data—reducing model complexity and improving generalisability by eliminating irrelevant predictors [32]. Additionally, the selection of a baseline window from -0.1 to 0 seconds relative to stimulus onset provided an effective normalisation window, commonly used in neuroscience to measure spontaneous neuron activity prior to stimulus presentation, thus enabling clear detection of stimulus-related changes in firing rates [33]. Despite these strengths, computational limitations prevented a full analysis of all vision- and choice-selective neurons, which may affect the strength and specificity of results derived from further analysis of NP data [34]. Moreover, the difference between our baseline window and that of Steinmetz et al. (2019) (-0.2 to 0 seconds), as well as our choice of ElasticNet over reduced-rank regression, may contribute to future discrepancies between our results and theirs [35]. Future work will aim to expand computational resources to fully evaluate neuron selectivity across all event types, including vision and choice, thereby maximising the analytical potential of kernel regression methodologies [36] [37].

5.5 Visualisation of Spikes

The optimal approach to determine the global coordinates of the spikes is the Euler-based neuron spike localisation method equipped with the AMSGRrad [38]. During the training process, it is found that the algorithm automatically sets z to zero, which is not expected coordinate for z . The algorithm tries to find the most easiest way to complete task, but the result is physically meaningless in the real world [39]. Therefore, the statistically reasonable estimation of z_c in terms of provided x_c and y_c coordinates can ensure the algorithm will not set z to zero initially, and the punishment system is also introduced for preventing the algorithm to make unreasonable estimation [40]. However, due to limited computational power, only a certain amount of data is processed and visualised. To solve this limitation, supercomputers can be used in the future. With their computational speed, more if not all the neuronal spikes could be visualised. Moreover, significant improvement in the effectiveness of the training algorithm for obtaining the optimal 3D coordinates is also expected.

6 Conclusion

6.1 Summary

In conclusion, this report demonstrates a novel computational pipeline that transforms NP electrophysiological data into a three-dimensional visualisation of neuronal activity in the mouse brain. The spikes are assigned with unique cluster IDs and processed using discussed statistical tests and Gaussian-based smoothing techniques to obtain the optimal neuronal responses. With the application of the Euler-based neuron spike localisation method equipped with AMSGrad optimizer, the optimal global coordinates of the spikes can be achieved, which further visualised in the brainrender. The different neurons, including action neurons and vision neurons, are visualised also in the brainrender. Although the 3D visualisation computational pipeline is exciting, a couple of limitations should also be stated. Firstly, the proposed filtering process should be tested for robustness with raw NP data rather than with just the pre-organised dataset provided by Steinmetz et al. Aside from that, only one folder out of 30 folders were run for the visualisation due to the limitation of the computational power. With the utilisation of advanced computers in the future, the entire dataset can be processed and visualized, which sustainably emphasizes the validity of results obtained in this project.

6.2 Future Work

Building on the encouraging results, future work on this study is also evident. In the future, the pipeline can be extended to process fully raw Neuropixel datasets rather than the pre-organised data, testing its generalisability and localisation methods in real-world applications. Additionally, current 3D visualisation in the Allen CCF coordinate can also be integrated with AR platforms like ARKit, ARCore in the future. By calibrating the coordinate systems using robust tracking methods to align virtual models with user’s physical environment, this potential can offer AR experiences for doctors to 3D visualise the locations of the spikes effectively for academic and clinical researches.

7 Appendix

7.1 Project management

The Gantt chart shows the timeline for this project from September 2024 through June 2025, which reflects the development of the entire project. Because of the difficulties in the stage of debugging and data processing, it takes a chronic time to develop into the next stage. For example, solving code problems in stages, including the organization and processing of data for

using in the visualisation of spikes, kernel function, and visualisation stage, are significantly time-consuming. It is especially worth mentioning that in the writing of the Pitch and final report in the Spring stage, the communication within the team was smooth and the content was integrated in an orderly manner, showing a strong overall control and time management ability. Although the project involved many complex links and challenges, team collaboration is an effective way to solve problems. The high high-frequency communication and tacit division of labour also play a significant role (Figure 10).

Although one of team members gets sick and cannot contribute effectively, the rest team members work collaboratively for solving various problems and challenges. After he recovers, he starts contributing as much as he can. In the future, we will work together continuously to complete the brochure.

7.2 Project Management Lessons

7.2.1 key lesson 1

The first key lesson is the importance of communication. At the beginning of the project, the team was divided into two subgroups. One group took the responsibility of the 3D visualization, while the other group took the responsibility of the data replication. Due to the shortage of effective communication between subgroups, there are a lot of arguments occurring regularly. For tackling the issue, regular group meetings times increased from twice a week to once a week. After that, the occurrence of arguing reduces, and every individual in the group contributes to the group work effectively. Although conflicts about project development direction still exists, the entire group tries to solve these conflicts immediately without delaying for a chronic time. Therefore, high-frequency communication skill in a group work is essentially important.

7.2.2 key lesson 2

The second key lesson is fair distribution of teamwork. During the stage of coding, there are a lot of unexpected problems occurring, including the convergence error of the loss function and unexpected error of data filtering. The individual in this group has different skills. For example, some group members are good at coding, while the rest members take responsibility of editing text and making the plots for demonstration. Although debugging the code and solving related coding problems takes a long time, the overall progress of the project is not influenced significantly since we distribute the work to the individual based on their advantages. Therefore, the importance of fair distribution of teamwork is recognised, and this key lesson will be applied in the future group work.

7.2.3 key lesson 3

Finally, the third key lesson is wise time management. Although this is a one year project, we still need to manage the time wisely. Based on past experience of teamwork, it is difficult and challenging to complete the assignments with the satisfactory quality if the students do not start doing the projects early. For this group project, we allocate the time effectively and wisely, and we have sufficient amount of time before the deadline. Occasionally, due to bad time management skills, the arguments and conflicts in the group are inevitable. Some students may blame each other before the assignment deadline due to the incompleteness of the assignments. Therefore, it is believed that the wise time management not only can address potential conflicts inside the group, but also provides students with enough time for completing the assignments.

7.3 Availability of Code

The code for this project can be accessed through the following address:

[Y3 Group Project Github Code](#)

7.4 Other Supplementary Material

7.4.1 Toeplitz matrix

This is the Toeplitz vision predictor matrix, which can be used to model the time-lagged relationships between stimuli and responses.

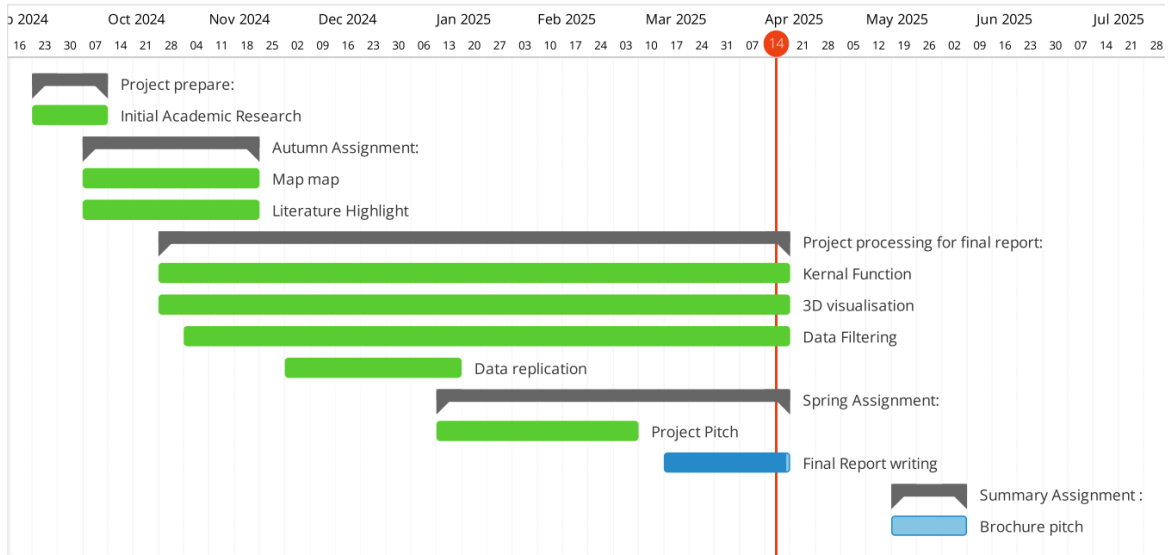


Figure 10: The plot for the project pitch Gantt chart.

Toepplitz Vision Predictor Matrix

		Columns (Lag from Stimulus)						
		-0.050	-0.045	0.000	0.395	0.400
Rows (Time)	0.000	0	0	1	0	0
	0.005	0	0	0	0	0
	0.010	0	0	0	0	0
	0.395	0	0	0	1	0
	0.400	0	0	0	0	1

Figure 11: The Toeplitz vision predictor matrix for modeling the time-lagged relationships between stimuli and responses.

Table 2: Description of variables in the ElasticNet objective function (Equation 2).

Variable	Description
y	Vector of observed neuronal firing rates (response variable).
X	Predictor matrix (combined vision, action, and choice predictors).
β	Vector of regression coefficients (weights for each predictor).
n	Number of observations (rows in data).
p	Number of predictors (columns in predictor matrix X).
α	Overall regularization strength (controls penalty magnitude).
ρ	ElasticNet mixing parameter, balancing L1 and L2 regularization. ($\rho = 1$: pure Lasso; $\rho = 0$: pure Ridge)
$\ \cdot\ _2^2$	Squared Euclidean norm (sum of squared values).
$\sum_{j=1}^p \beta_j $	L1 penalty (Lasso), encourages sparse coefficients.
$\sum_{j=1}^p \beta_j^2$	L2 penalty (Ridge), encourages coefficient stability.

References

- [1] Paul A. Yushkevich, Josien P. W. Pluim, Boštjan Likar, and Frans A. Gerritsen. 3d mouse brain reconstruction from histology using a coarse-to-fine approach. In Josien P. W. Pluim, Boštjan Likar, and Frans A. Gerritsen, editors, *Biomedical Image Registration*, pages 230–237. Springer, Berlin, Heidelberg, 2006.
- [2] Nicholas A. Steinmetz, Peter Zatka-Haas, Matteo Carandini, and Kenneth D. Harris. Distributed coding of choice, action and engagement across the mouse brain. *Nature*, 576:266–273, 2019.
- [3] Yufeng Liu et al. Neuronal diversity and stereotypy at multiple scales through whole brain morphometry. *Nature Communications*, 15(1):10269, nov 2024.
- [4] Julien Boussard, Erdem Varol, Hyun Dong Lee, Nishchal Dethé, and Liam Paninski. Three-dimensional spike localization and improved motion correction for neuropixels recordings. In *Proceedings of the 35th International Conference on Neural Information Processing Systems*, NIPS ’21, Red Hook, NY, USA, 2021. Curran Associates Inc.
- [5] Nicholas A. Steinmetz et al. Challenges and opportunities for large-scale electrophysiology with neuropixels probes. *Current Opinion in Neurobiology*, 50:92–100, jun 2018.
- [6] Marius Pachitariu et al. Fast and accurate spike sorting of high-channel count probes with Kilo-Sort. In *Advances in Neural Information Processing Systems*, volume 29. Curran Associates, Inc., 2016.
- [7] J. Jun, N. Steinmetz, J. Siegle, et al. Fully integrated silicon probes for high-density recording of neural activity. *Nature*, 551(7679):232–236, nov 2017.
- [8] Chun-Feng Shang et al. Real-time analysis of large-scale neuronal imaging enables closed-loop investigation of neural dynamics. *Nature Neuroscience*, 27(5):1014–1018, may 2024.
- [9] Q. Wang et al. The allen mouse brain common coordinate framework: A 3d reference atlas. *Cell*, 181(4):936–953.e20, may 2020.
- [10] G. Barbarino et al. Spectral properties of flipped Toeplitz matrices and computational applications. *Applied Mathematics and Computation*, 499:129408, july 2024.
- [11] S. Srinivasan and P. Deepalakshmi. EN-ETRM: ElasticNet regression model based malicious cyber-attacks prediction in real-time server. *Measurement: Sensors*, 25:100654, feb 2023.
- [12] I.S. Samanta et al. A hybrid approach for power quality event identification in power systems: Elasticnet regression decomposition and optimized probabilistic neural networks. *Heliyon*, 10(18):37975, may 2024.
- [13] Diederik P. Kingma and Jimmy Ba. Adam: A method for stochastic optimization. *CoRR*, abs/1412.6980, 2014.
- [14] John Duchi, Elad Hazan, and Yoram Singer. Adaptive subgradient methods for online learning and stochastic optimization. *Journal of Machine Learning Research*, 12(61):2121–2159, 2011.
- [15] Y. Wang et al. A novel structural adaptive discrete grey Euler model and its application in clean energy production and consumption. *Energy*, 323:135807, dec 2024.
- [16] H. Gunasekaran et al. Convergence of regular spiking and intrinsically bursting Izhikevich neuron models as a function of discretization time with Euler method. *Neurocomputing*, 350:237–247, jul 2019.
- [17] Federico Claudi, Adam L. Tyson, Luigi Petrucco, Troy W. Margrie, Ruben Portugues, and Tiago Branco. Visualizing anatomically registered data with brainrender. *eLife*, 10:e65751, 2021.
- [18] Naomi P. Friedman and Trevor W. Robbins. The role of prefrontal cortex in cognitive control and executive function. *Neuropsychopharmacology*, 47(1):72–89, jan 2022.
- [19] P. Shamash, M. Carandini, K.D. Harris, and N.A. Steinmetz. A tool for analyzing electrode tracks from slice histology. *bioRxiv*, oct 2018. Preprint.
- [20] A. Alegria, A. Joshi, J. O’Brien, and S. B. Kodandaramaiah. Single neuron recording: progress towards high-throughput analysis. *Bioelectronic Medicine (London)*, 3(3):33–36, 2020.
- [21] R. H. Roth and J. B. Ding. From neurons to cognition: Technologies for precise recording of neural activity underlying behavior. *BME Frontiers*, 2020:7190517, 2020.
- [22] B. Burle, L. Spieser, C. Roger, L. Casini, T. Hasbroucq, and F. Vidal. Spatial and temporal resolutions of eeg: Is it really black and white? a scalp current density view. *International Journal of Psychophysiology*, 97(3):210–220, 2015.
- [23] B. J. Edelman, N. Johnson, A. Sohrabpour,

- S. Tong, N. Thakor, and B. He. Systems neuro-engineering: Understanding and interacting with the brain. *Engineering*, 1(3):292–308, 2015.
- [24] X. Zeng and G. Li. A supervised clustering and classification algorithm for mining data with multiple labels. In *Proceedings of the 4th International Conference on Computer and Information Technology (CIT 2003)*, pages 527–532. IEEE, dec 2003.
- [25] G.L. Gerstein and D.H. Perkel. Simultaneously recorded trains of action potentials: analysis and functional interpretation. *Science*, 164(3881):828–830, may 1969.
- [26] W. Gao et al. Real-time filtering method based on neuron filtering mechanism and its application on robot speed signals. In *Lecture Notes in Electrical Engineering*, pages 971–978. Springer, dec 2013.
- [27] Y. Zhang et al. A novel hybrid deep learning model for sensor-based human activity recognition. *Sensors*, 20(1):299, 2020.
- [28] A.B. Wiltschko et al. Mapping sub-second structure in mouse behavior. *Neuron*, 110(3):395–410, feb 2019.
- [29] Y. Bai et al. A neuron-based kalman filter with nonlinear autoregressive model. *Sensors*, 20(1):299, jan 2020.
- [30] A. de Cheveigné and I. Nelken. Filters: When, why, and how (not) to use them. *Neuron*, feb 2019.
- [31] A.J. Izenman. Reduced-rank regression for the multivariate linear model. *Journal of Multivariate Analysis*, 5:248–264, jun 1975.
- [32] Hui Zou and Trevor Hastie. Regularization and variable selection via the elastic net. *Journal of the Royal Statistical Society: Series B (Statistical Methodology)*, 67(2):301–320, 2005.
- [33] Mark M Churchland, Myron Y Byron, John P Cunningham, Leo P Sugrue, Marlene R Cohen, Greg S Corrado, William T Newsome, Andrew M Clark, Pouya Hosseini, Yoram T Wong, et al. Stimulus onset quenches neural variability: a widespread cortical phenomenon. *Nature Neuroscience*, 13(3):369–378, 2010.
- [34] Yuxin Li et al. A review on machine learning applications for sustainable construction supply chain performance. *Journal of Cleaner Production*, 367:132964, sep 2022.
- [35] J. Ashe and A.P. Georgopoulos. Movement parameters and neural activity in motor cortex and area 5. *Cerebral Cortex*, 4:590–600, nov 1994.
- [36] I.M. Park, M.L.R. Meister, A.C. Huk, and J.W. Pillow. Encoding and decoding in parietal cortex during sensorimotor decision-making. *Nature Neuroscience*, 17:1395–1403, oct 2014.
- [37] L. Paninski, S. Shoham, M.R. Fellows, N.G. Hatsopoulos, and J.P. Donoghue. Superlinear population encoding of dynamic hand trajectory in primary motor cortex. *Journal of Neuroscience*, 24:8551–8561, sep 2004.
- [38] Y. LeCun et al. Learning mid-level features for recognition. *Neural Networks*, 23(6):657–666, aug 2010.
- [39] T. Kim et al. Distinct roles of parvalbumin- and somatostatin-expressing interneurons in working memory. *Neuron*, 109(12):1967–1978.e4, jun 2021.
- [40] C. Olah et al. Feature visualization. *Distill*, nov 2017.